energies

MDPI

Article

Effects of Crystal Morphology on the Hot-Carrier Dynamics in Mixed-Cation Hybrid Lead Halide Perovskites

Daniele Catone [1,*], Giuseppe Ammirati [1,2], Patrick O'Keeffe [3], Faustino Martelli [4], Lorenzo Di Mario [1,5], Stefano Turchini [1], Alessandra Paladini [3], Francesco Toschi [3], Antonio Agresti [2], Sara Pescetelli [2] and Aldo Di Carlo [1,2]

1 Istituto di Struttura della Materia (ISM-CNR), Division of Ultrafast Processes in Materials (FLASHit), Area della Ricerca di Roma Tor Vergata, Via del Fosso del Cavaliere 100, 00133 Rome, Italy; giuseppe.ammirati@ism.cnr.it (G.A.); l.di.mario@rug.nl (L.D.M.); stefano.turchini@ism.cnr.it (S.T.); aldo.dicarlo@ism.cnr.it (A.D.C.)
2 CHOSE (Centre for Hybrid and Organic Solar Energy), Department of Electronic Engineering, University of Rome Tor Vergata, Via del Politecnico 1, 00133 Rome, Italy; antonio.agresti@uniroma2.it (A.A.); pescetel@uniroma2.it (S.P.)
3 Istituto di Struttura della Materia (ISM-CNR), Division of Ultrafast Processes in Materials (FLASHit), Area della Ricerca di Roma 1, 00015 Monterotondo Scalo, Italy; patrick.okeeffe@ism.cnr.it (P.O.); alessandra.paladini@cnr.it (A.P.); francesco.toschi@cnr.it (F.T.)
4 CNR-IMM, Area della Ricerca di Roma Tor Vergata, 100 Via del Fosso del Cavaliere, 00133 Rome, Italy; faustino.martelli@cnr.it
5 Zernike Institute for Advanced Materials, University of Groningen, Nijenborgh 4, 9747 AG Groningen, The Netherlands
* Correspondence: daniele.catone@cnr.it

Citation: Catone, D.; Ammirati, G.; O'Keeffe, P.; Martelli, F.; Di Mario, L.; Turchini, S.; Paladini, A.; Toschi, F.; Agresti, A.; Pescetelli, S.; et al. Effects of Crystal Morphology on the Hot-Carrier Dynamics in Mixed-Cation Hybrid Lead Halide Perovskites. *Energies* **2021**, *14*, 708. https://doi.org/10.3390/en14030708

Academic Editor: Senthilarasu Sundaram
Received: 29 December 2020
Accepted: 28 January 2021
Published: 30 January 2021

Abstract: Ultrafast pump-probe spectroscopies have proved to be an important tool for the investigation of charge carriers dynamics in perovskite materials providing crucial information on the dynamics of the excited carriers, and fundamental in the development of new devices with tailored photovoltaic properties. Fast transient absorbance spectroscopy on mixed-cation hybrid lead halide perovskite samples was used to investigate how the dimensions and the morphology of the perovskite crystals embedded in the capping (large crystals) and mesoporous (small crystals) layers affect the hot-carrier dynamics in the first hundreds of femtoseconds as a function of the excitation energy. The comparative study between samples with perovskite deposited on substrates with and without the mesoporous layer has shown how the small crystals preserve the temperature of the carriers for a longer period after the excitation than the large crystals. This study showed how the high sensitivity of the time-resolved spectroscopies in discriminating the transient response due to the different morphology of the crystals embedded in the layers of the same sample can be applied in the general characterization of materials to be used in solar cell devices and large area modules, providing further and valuable information for the optimization and enhancement of stability and efficiency in the power conversion of new perovskite-based devices.

Keywords: perovskite; ultrafast; hot-carriers; solar cell

1. Introduction

Hybrid lead halide perovskites exhibit very promising optoelectronic properties, such as long carrier lifetime [1], high absorption coefficients in the visible spectral range, optimal carrier diffusion [2] and charge transport [3,4]. These outstanding features have designated the hybrid perovskites as one of the best candidates for active materials in solar cell applications [5]. Since 2006, hybrid perovskites have been studied to produce highly efficient perovskite-based solar cells (PSCs), starting with a power conversion efficiency (PCE) of 2.19% in the initial studies [6] and reaching a present-day value of 25.5% [7]. This tremendous increase in performance was possibly thanks to intense research activity

worldwide that led to the optimization of perovskite material synthesis [8] and of charge carrier extraction [5]. Despite the high PCE obtained by the methylammonium lead iodide perovskite (MAPI) [9], which is the most widely used active material in PSCs, the main obstacle to a widespread commercial application remains its high sensitivity to ambient conditions, such as oxygen, moisture and heat that strongly undermine the stability over time of this material [10,11]. For this reason, efforts have been directed into the development of new perovskite compositions, mixing different cations and halides with the aim to minimize the main instability factors. Indeed, the category of the mixed-cation hybrid lead halide perovskites has proven to be one of the most thermally stable in composition and the materials synthetized with methylammonium, formamidinium and cesium as cations have demonstrated an improved thermal and structural stability [10,12].

Ultrafast pump-probe spectroscopies have proved to be an important tool for the investigation of charged carrier dynamics in perovskite materials and perovskite-based devices [13–15]. The in-depth study of the physics behind the ultrafast processes, such as carrier excitation, relaxation, recombination and transport, discloses the optoelectronic properties of these materials and the correlation between crystal structure and energy transfer. In particular, the investigation of charge generation and transfer processes, carrier thermalization and cooling, provides crucial information on the ultrafast dynamics of the carriers in perovskites, fundamental in the development of new PSCs with tailored photovoltaic properties. Thus, the study of the main processes that involve the energy-loss dynamics of hot-carriers in the first hundreds of femtoseconds after the excitation is crucial in defining their contribution to the PCE once they have come into thermal equilibrium with the lattice [16]. The excited carriers achieve thermal equilibrium with the lattice and the environment thanks to thermalization (carrier-carriers scattering) and cooling (carrier-phonon scattering) [15,17,18] that occur on a time scale ranging from tens of femtoseconds to hundreds of picoseconds and imply an exchange of energy among carriers and between carriers and phonons, creating a thermal distribution of carriers at a time-dependent specific temperature (T_C). The possibility of slowing carrier cooling in perovskite materials has garnered great interest thanks to the hope of exploiting this process to design hot-carrier solar cells [18,19], with the aim of reducing the energy loss before carrier extraction and hence improving PSC efficiency [20]. Unfortunately, the timescale of the carrier cooling strongly depends on the excess energy with respect to the band edge and on the initial excitation carrier density. The latter should be higher than 5×10^{17} cm^{-3} [19] to induce the required long cooling times (tens to hundreds of picoseconds) for practical hot-carrier extraction. These conditions are clearly far from those that are obtained under a single sun illumination [19] and therefore not directly relevant for practical use with PSC devices.

The optical experimental techniques needed to study hot-carrier cooling and carrier transport require high temporal resolution at the fs/ps timescales. A number of optical pump-probe processes can be used to achieve such resolutions including transient absorption and reflection (TA/TR) [18,21,22] (Figure 1), transient absorption microscopy [23], and 2D electronic spectroscopy [17], as well as time-resolved photoluminescence (TRPL) [24]. These techniques have been extensively applied to a wide range of traditional halide perovskites such as $MAPbI_3$, $FAPbI_3$, $CsPbI_3$ in a range of different morphologies from thin film layers, to nanocrystals, to full solar cell architectures, studying many of the processes discussed above [19]. On the other hand, the newly developed mixed-cation hybrid lead halide perovskite $Cs_{0.06}(MA_{0.17}FA_{0.83})_{0.94}Pb(I_{0.83}Br_{0.17})_3$ (CsMAFA) [12] is much less studied using those techniques although some works including the study of carrier transport by near infrared TA/TR [25], long-lived charge carriers [26] and the effect of halide doping on hot carrier cooling by using TA [27] have been recently published. However, to the best of our knowledge the dependence of hot-carrier cooling on morphology has not been studied for this material.

In this work, we investigate the dependence of carrier thermalization and cooling on the morphology of the mixed-cation hybrid lead halide perovskite CsMAFA as a function

of the excitation energy with low photoexcited carrier densities (about 8.0×10^{16} cm^{-3}). In order to isolate the effect of morphology of the perovskite, two different sample structures were studied: Glass + FTO/c-TiO_2/m-TiO_2/CsMAFA (Meso-Capping) and Glass + FTO/c-TiO_2/CsMAFA (Solo-Capping) where FTO is the fluorinated tin oxide used for transparent conducting electrodes, c-TiO_2 is compact TiO_2, and m-TiO_2 is mesoporous TiO_2. In this way, we study crystal morphologies that are directly relevant for operating solar cells but without the possible modifications of the dynamics introduced by the perovskite/hole transport layer interface, which is present in a complete PSC [28]. The Meso-Capping sample has a layer design of a typical mesoscopic PSC except for the hole transport layer and the back electrode. In particular, the Meso-Capping sample presents a capping layer of large-sized perovskite crystals of about 600 nm (layer thickness of about 480 nm) and a mesoporous layer composed of small-sized 20−40 nm crystals, spatially restrained within the m-TiO_2 layer (layer thickness of about 130 nm) [29]. On the other hand, the Solo-Capping sample presents only a CsMAFA bulk layer, namely a capping layer (layer thickness of about 400 nm) [30,31], deposited on top of a compact layer of TiO_2. A schematic representation of the sample structures is reported in Figure 2a. The comparative study of the results on the samples with and without the m-TiO_2 layer has allowed us to show how the size of small crystals of CsMAFA formed in the mesoporous layer affects the ultrafast dynamics of the thermalization and cooling of the excited carriers with respect to that of the large crystals in the capping layer. The excitation pump energies were selected to be below the opening of the second bandgap of the CsMAFA that, in an analogy with MAPI, is expected to lay above 2.5 eV [32]. In this way, the superposition of different energy-loss processes due to the filling of two different conduction bands and the consequent non-uniform energy redistribution in the generation of hot carriers were avoided.

2. Materials and Methods

The preparation of the Meso-Capping sample begins with a patterned FTO-coated glass substrate that was first washed using a liquid detergent, rinsed with deionized water, and then sonicated in acetone and isopropyl alcohol (IPA) for 10 min for each step. The spray pyrolysis technique was used to realize the c-TiO_2 blocking layer by employing a solution of acetylacetone (2 mL), titanium diisopropoxide (3 mL) and ethanol (45 mL) at 460 °C. The subsequent thin m-TiO_2 porous film (~150 nm) was obtained by spin coating a TiO_2 paste (Dyesol 18 NR-T paste diluted in ethanol 1:5 in wt.) on to the FTO/c-TiO_2 substrate at 3000 rpm for 20 s and then by sintering it at 460 °C for 30 min in air. The CsMAFA layer was deposited in a nitrogen filled glovebox with a one-step deposition and antisolvent method [33,34]. All of the organic cations were acquired from Dyesol, while the lead compounds were obtained from TCI and CsI was purchased from abcr GmbH. The precursor CsMAFA solution was prepared by dissolving, with the molar ratio suggested by Saliba et al. [12] a mixture of lead(II) iodide (PbI_2), lead(II) bromide ($PbBr_2$), methylammonium bromide (MABr), formamidinium iodide (FAI) and cesium iodide (CsI) in a solvent mixture of anhydrous N,N-dimethylformamide (DMF) and dimethylsulfoxide (DMSO) in a 3:1 ratio (v:v). The resulting mixed perovskite precursor solution was spin coated onto the FTO/c-TiO_2/m-TiO_2 substrate by using a two-step sequence consisting of 1000 and 5000 rpm cycles for 10 and 30 s, respectively. The antisolvent (200 µL of chlorobenzene) was dropped onto the substrate during the second spinning step onto the sample, 7 s prior to the end of the program. Finally, the substrates were annealed at 100 °C for 1 h. In the case of the Solo-Capping sample, the mixed perovskite solution was spin-coated on to an FTO/c-TiO_2 substrate without the mesoporous layer.

The fast transient absorbance spectroscopy (FTAS) measurements were performed by using a femtosecond laser system equipped with a chirped-pulse amplifier (800 nm, 4 mJ, 1 kHz, 35 fs) seeded by a Ti:Sapphire oscillator. The pump pulses were produced by the output of an optical parametric amplifier that permitted a complete tunability in the 240–1600 nm wavelength range. The probe pulse was a white light supercontinuum beam (360–780 nm) that was generated in a commercial TA spectrometer (FemtoFrame II,

IB Photonics) by focusing an 800 nm pulse (~3 μJ) into a rotating CaF_2 crystal. The pump pulse was focused (spot diameter of about 400 μm) onto the sample with variable energy and fluence of 2−10 μJ/cm^2. In this way, the differences in sample absorbance when excited or not by the pump, i.e., the transient absorbance ΔA (expressed in mOD), were measured as a function of the pump-probe delay time. The instrument response function (IRF) was estimated to be about 50 fs. Figure 1 reports the schematic representation of the FTAS setup used to perform the pump-probe measurements. Further details of the experimental set-up can be found in previous publications [35–37].

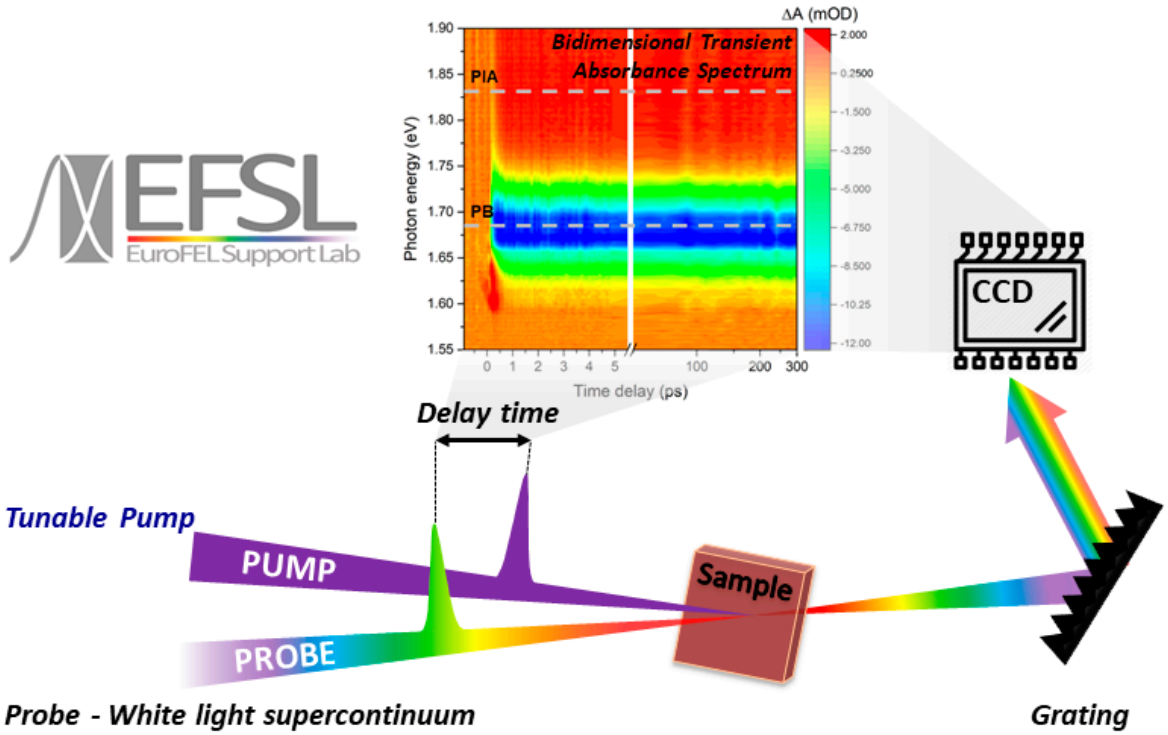

Figure 1. Schematic representation of the fast transient absorbance spectroscopy (FTAS) setup used to perform the pump-probe measurements.

3. Results and Discussion

3.1. Transient Absorbance Spectra

The TA spectra were all acquired in transmission with different pump photon energies (E_p = 2.50 eV, 2.25 eV and 2.00 eV) and a probe pulse in the 1.55−2.40 eV energy range. The Meso-Capping sample was alternately illuminated from each side (see the scheme in Figure 2a) with the aim of exciting preferentially the small crystals of the mesoporous layer (Meso side) or the large crystals of the capping layer (Capping side). In this way, it was possible to investigate the differences in the hot-carrier dynamics induced by the different morphology of the perovskite crystals. On the other hand, the Solo-Capping sample was used as a reference for the results obtained from the Meso-Capping sample, also accounting for the different penetration depth of the pump as a function of its energy. Penetration depths of 60 nm at 2.5 eV, 100 nm at 2.25 eV and 170 nm at 2.00 eV for a film of CsMAFA, defined as 1/e reduction of the incident intensity, were estimated at the used experimental pump energies [38]. The Solo-Capping sample was illuminated from the capping layer side for all pump energies employed since it showed the same TA signals when illuminated from both sides.

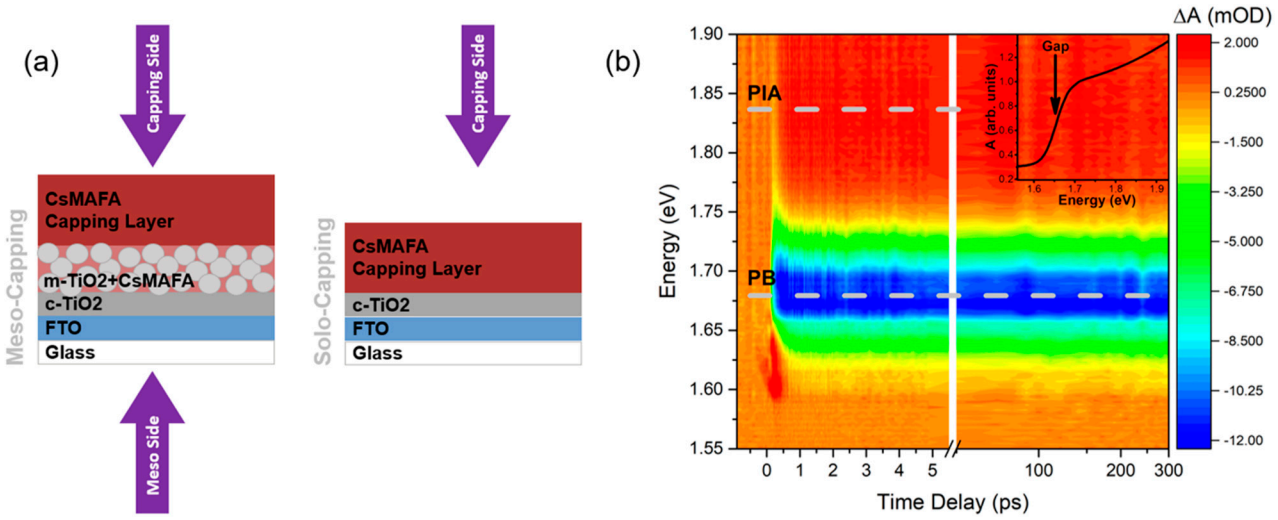

Figure 2. Schematic representations of the layer designs of (**a**) the Meso-Capping and Solo-Capping samples. The arrows indicate the side from which the samples were illuminated by the pump and probe pulses. (**b**) False-color map of the absorbance difference ΔA (expressed in mOD) as a function of the probe energy (*y* axis) and the pump-probe time delay between (*x* axis) obtained for the Meso-Capping sample with E_p = 2.25 eV impinging on the Meso side with a fluence of 4.00 μJ/cm^2. Inset: absorption spectrum of the Meso-Capping sample.

Figure 2b shows the false-color map of the absorbance difference ΔA (expressed in mOD) as a function of the probe energy (*y* axis) and the pump-probe time delay between (*x* axis) obtained for the Meso-Capping sample with E_p = 2.25 eV impinging on the Meso side with a fluence of 4.00 μJ/cm^2 that corresponds to an initial carrier density of about 8.00 × 10^{16} cm^{-3}. The TA map presents a negative signal at 1.66 eV assigned to the photobleaching (PB) of the CsMAFA band gap [39–41], in agreement with the absorption spectrum acquired with an ultraviolet–visible (UV–Vis) spectrophotometer (Jasco V-630) and reported in the inset of Figure 2b. In similar experiments performed on the more widely studied MAPI, the weak and broad positive large band of photoinduced absorption (PIA) in the 1.75 to 1.90 eV range is typically assigned to band gap renormalization effects [22] and population of newly excited states induced by the pump [42]. In any case, the features of the TA map, characterized by PB and PIA signals, are due to different spectral contributions that act in different ways as the time elapses after the excitation and that cannot be considered independently. The TA spectra were acquired up to 2.40 eV (here are reported only those up to 1.90 eV) because the thickness of the sample (480 nm of Capping layer and 130 nm of Meso layer) prevented the transmission of the probe at higher energies as it was completely absorbed by the CsMAFA. The reduction of the thickness was not considered to be an ideal solution to solve this problem because the aim of this work was to demonstrate the capability of performing ultrafast transient absorbance investigations on samples with the same layer design and thickness of solar cells [43] or large area modules [44]. Moreover, this limited probe spectral range proved to be sufficient to follow the carrier thermalization and cooling processes that occurred through carrier–carrier and carrier–phonon scattering on a time scale ranging from tens/hundreds of femtoseconds [15,17] to picoseconds [22], respectively.

In Figure 3, the TA spectra of the Meso-Capping sample illuminated from the Meso and Capping sides by different E_p (2.50 eV, 2.25 eV, 2.00 eV) are reported, together with the TA spectra of the Solo-Capping sample obtained in the same experimental conditions. All spectra were acquired at 100 ps of time delay, when the thermalization and cooling processes were essentially terminated. Moreover, the pump fluences were carefully selected in order to excite the same carrier density for the different pump energies, namely about 8.0 × 10^{16} cm^{-3}.

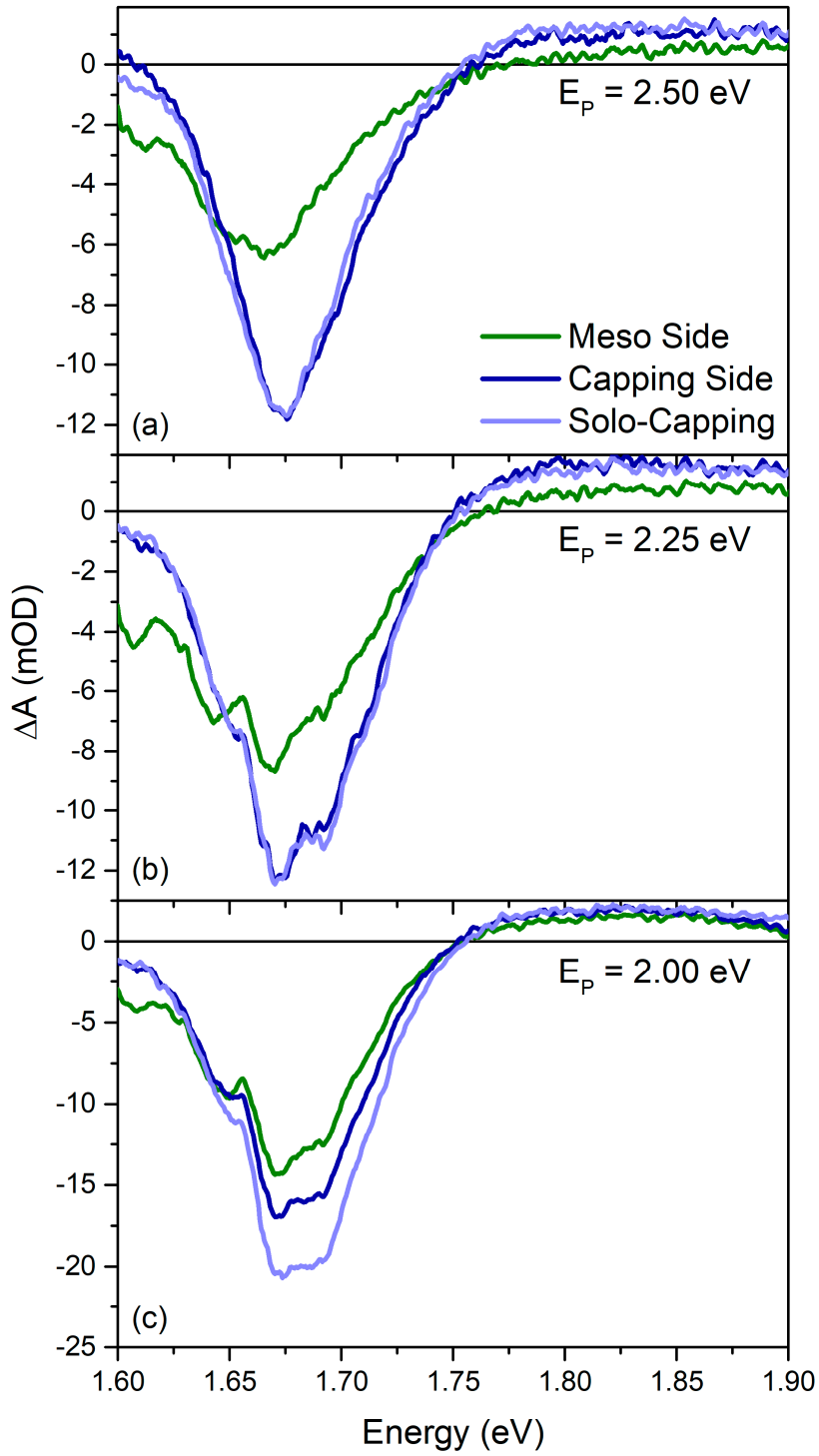

Figure 3. Transient absorption (TA) spectra of the Meso-Capping sample illuminated from the Meso and Capping sides, and TA spectra of the Solo-Capping sample, acquired at a time delay of 100 ps and with E_p at (**a**) 2.50 eV, (**b**) 2.25 eV and (**c**) 2.00 eV. The peaks and features present at energies below 1.65 eV are artifacts due to the fluctuations of the white-light supercontinuum probe near the low-energy edge.

The TA spectra of the Meso-Capping sample acquired with E_p = 2.50 eV and illuminating the Meso or the Capping side (see Figure 3a), present differences in width and position that are directly connected to the different crystal morphology of the layers. In fact, the very close agreement between the TA spectrum of the Meso-Capping sample excited from

the capping side and the TA spectrum obtained for the Solo-Capping sample, strongly indicates that the pump pulse was completely absorbed within the thickness of the capping layer. For the same reason, the TA spectrum acquired by illuminating the Meso-Capping sample from the Meso side can be considered to have been mainly due to the small Cs-MAFA crystals in the mesoporous layer. Nonetheless, the penetration of a small quantity of pump light through the Capping side cannot be excluded due to the smaller thickness of the Meso layer (130 nm). However, the different shape and the lower intensity of the TA spectrum obtained from the Meso side can be explained by the lower density of CsMAFA embedded in the m-TiO_2 and the higher scattering induced by the nanostructuring of the mesoporous layer. These differences demonstrate a clear dependence of the TA signals on which side of the Meso-Capping sample is illuminated with E_p = 2.50 eV. The influence of the FTO and TiO_2 on the spectral differences between the Meso and Capping sides was excluded by the absence of signals obtained from a sample without CsMAFA.

With these considerations in mind, the different minima of the PB signals obtained for the Meso (1.665 eV) and the Capping (1.675 eV) side can be discussed in terms of the different dimensions of the excited crystals. In particular, the lower energy value of the minimum of the PB signal for the small crystals in the mesoporous layer was in contradiction with the results obtained for other hybrid halide perovskites [15,16,45]. This discrepancy can be explained by a possible variation in the stoichiometry of the small crystals in the mesoporous layer due to illumination-induced ion diffusion and halide segregation that can slightly shift the band gap of the CsMAFA [41,46,47]. On the other hand, the energy value of the minimum of the PB was only in part related to the effective energy of the material band gap due to the transient nature of the signal acquired. A small shift of the PB can be influenced by other factors that change the line shape of the TA spectrum, such as band gap renormalization effects or excitonic states near the gap [22]. In any case, the small difference in the relative value of the PB minima did not affect the temporal analysis of the T_C.

In the light of these considerations, the results obtained by exciting the samples with E_p at 2.25 eV (Figure 3b) and 2.00 eV (Figure 3c) can be understood by considering the longer penetration depth of the pump with the decrease of its energy and the consequent excitation of different portions of the sample layers that results in a different sensitivity to the morphology of the CsMAFA crystals. In particular, with the E_p = 2.25 eV the TA spectra still present differences similar to those obtained with E_p = 2.50 eV, as shown in Figure 3b. In fact, the TA spectrum obtained from the Meso-Capping sample, exciting the Meso side, is very similar to the spectrum collected from the same side with E_p = 2.50 eV. In fact, the TA spectrum extends at lower energies beyond 1.60 eV and is still less intense than the TA spectrum obtained by optically pumping from the Capping side. Moreover, the similar line shapes of the TA spectra collected from the Solo-Capping sample and from the Capping side of the Meso-Capping sample again confirm the sensitivity of the TA signal to the contribution of the small crystals, even though the line shape and the minimum of the PB signals in this case are similar among all the spectra. This demonstrates a non-negligible contribution of the capping layer to the TA spectrum collected form the Meso side, which increases further in intensity with E_p = 2.00 eV. We point out that the peaks and features present at energies below 1.65 eV are artifacts due to the fluctuations of the white-light supercontinuum probe near the low-energy edge.

In the case of the pump at 2.00 eV, the TA spectra of both samples are very similar to each other except for their intensity. In fact, the TA spectrum of the Meso-Capping sample collected illuminating the Capping side is less intense than the TA spectrum obtained from the Solo-Capping sample. This feature indicates that in the former sample the pump also propagates through the mesoporous layer. This fact results in a stronger scattering of the light that results in a weaker transient signal. Thus, the pump at 2.00 eV, passing through the sample partially or totally, induces a PB signal influenced by the contributions of both the mesoporous and capping layers of CsMAFA.

3.2. Carrier Temperature Dynamics

The present results clearly demonstrate the sensitivity of the FTAS to the dimensions and morphology of the perovskite crystals embedded in the adjacent capping and mesoporous layers. Furthermore, this sensitivity grants the possibility to follow and investigate the dynamics of the carrier energy-loss processes that occur in crystals of different sizes directly by examining a solar cell device. For this reason, any differences of TA spectra acquired on a temporal scale compatible with thermalization and cooling processes, can therefore be discussed by considering how the morphology of the crystals can influence the dynamics of hot-carriers and their temperature as a function of the pump energy. In fact, the comparison of the TA spectra, obtained for the Meso-Capping sample excited with E_p = 2.50 eV from the Meso and Capping side at a time delay of 400 fs and reported in Figure 4, reveals further differences. In fact, the TA spectrum acquired exciting the sample from the Meso side exhibits a PB signal with a longer high-energy tail (green line) with respect to that obtained when pumping from the Capping side (blue line). This is due to a different T_C. In particular, the broader tail of the Meso side, corresponding to a higher T_C, confirms that the small crystals in the mesoporous layer preserve the temperature of the carriers for a longer time after the excitation than the large crystals in the capping layer [15,18]. This is likely due to a slower decay of the optical phonons into acoustic phonons (acoustic phonon bottleneck) due to the lower thermal conductivity in small-sized crystals [48]. The estimation of the T_C was obtained by using a simple Maxwell–Boltzmann function to fit the high-energy tail (grey lines in Figure 4 and red lines in the inset of Figure 4) of the PB signal extracting the temperature of the carriers after the initial pump excitation (inset of Figure 4) [15,18,21,22].

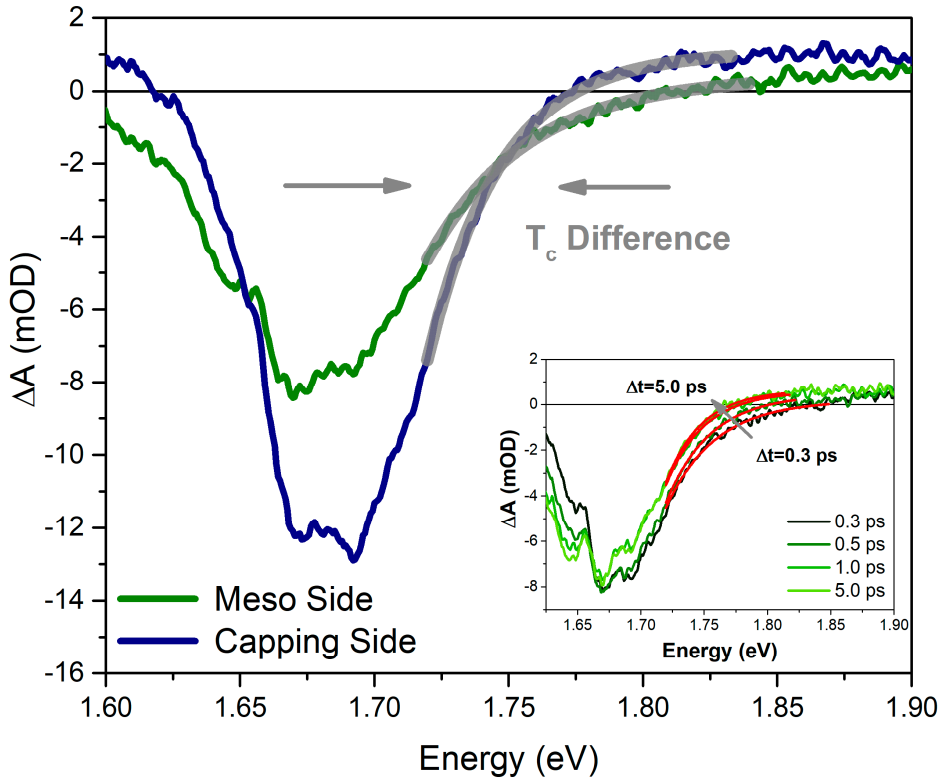

Figure 4. TA spectra of the Meso-Capping sample illuminated from the Meso and Capping sides acquired at a time delay of 400 fs and with E_p = 2.50 eV along with the best fit (grey lines) of the high-energy tails used to estimate the carrier temperature. Inset: TA spectra at different pump-probe time delay (from 0.3 to 5 ps) for the Meso-Capping sample illuminated from the Meso side and the best fits (red lines) obtained for the high-energy tails.

Figure 5a–c shows the T_C for the Meso-Capping sample excited from both sides and the Solo-Capping sample for the selected pump energies and as a function of time delay (from 0.25 to 5 ps), together with an exponential fit to guide the eyes. The T_C obtained by exciting the Meso side of the Meso-Capping sample is at any time delay higher than in the Capping layers, regardless of the pump energy. This behavior is explained by a slower overall carrier thermalization and cooling rate for the small crystals in the mesoporous layer than in the large crystals of the capping layer [15,18]. Moreover, the evident similarity of the T_C estimated for the two Capping layers (Meso-Capping and Solo-Capping samples) at the lowest pump photon energy confirms the poor sensitivity of the pump at this energy to the morphology of the crystals, as already discussed when comparing the TA spectra reported in Figure 4. In all the cases studied, the initial T_C increases with the pump photon energy (Figure 5d), as expected because of the increase of excess energy supplied by the pump to the photoexcited carriers. Accordingly, the great similarity between all TA spectra obtained with E_p = 2.00 eV (Figure 5c) is explained by the higher thickness of the capping layer with respect to the mesoporous layer that induce an overall transient response that retains the dynamics of the large crystals more than the small ones. Moreover, at time delays longer than 5 ps T_C values are roughly constant (the line shape of the PB signal remains substantially unaltered), giving evidence that the thermalization and cooling processes are largely terminated.

All the T_C dynamics reported in Figure 5 start from 250 fs because, before this time delay, the dominant process for the exchange of energy is the carrier thermalization, which consists of non-equilibrium process, during which it is not possible to define a temperature for the carrier distribution [15,18], namely the line shape of the high-energy tail of the PB signal cannot be reasonably fit by an exponential Maxwell–Boltzmann function. Moreover, all the sub-picosecond dynamics of T_C show very similar decay rate constants (200–400 fs) [49], regardless of the crystal morphology, which principally affects the cooling process. With these considerations in mind and assuming that the initial energy of the excited carrier distribution depends only on the energy excess supplied by the pump with respect to the gap, the higher initial T_C obtained for the small crystals can be explained by a slower thermalization and cooling of the excited carriers that occurs at shorter time delays with respect to the large crystals of the capping layer, demonstrating that the small crystals in the mesoporous layer preserve the temperature of the carriers for a longer time after the excitation at different energies [15].

It should be noted that at the initial carrier density (8.0×10^{16} cm^{-3}) studied in this work, many of the processes usually contributing to slowing the carrier cooling can be neglected. For example, Yang et al. [22] sets a limit of 5×10^{17} cm^{-3} for the onset of the hot phonon bottleneck in lead halides perovskites. Beyond this limit the carriers can reabsorb energy from the hot phonon population of the lattice thus slowing cooling to several picoseconds or more. At even higher carrier densities (>10^{19} cm^{-3}) the Auger effect becomes dominant slowing down the carrier cooling to tens or even hundreds of picoseconds and making it impossible to analyse the carrier cooling properly [20,50]. On the other hand, at low initial carrier densities (<5×10^{17} cm^{-3}) the carrier cooling rates are typically in the time scale of hundreds of femtoseconds or less, as has been shown in a wide range of perovskites [19]. In contrast, the carrier thermalization times in these materials is much less studied due to the high temporal resolution required for such investigations. The few studies on this process for $MAPbI_3$ and $MAPbBr_3$ revealed a thermalization rate of less than 10 to 100 fs at an initial excitation carrier density of 10^{18}–10^{19} cm^{-3} [17,51]. As the thermalization characteristic rate times increase as the carrier density decreases, with the initial carrier densities used in this work, the rates of carrier thermalization and cooling processes approach each other.

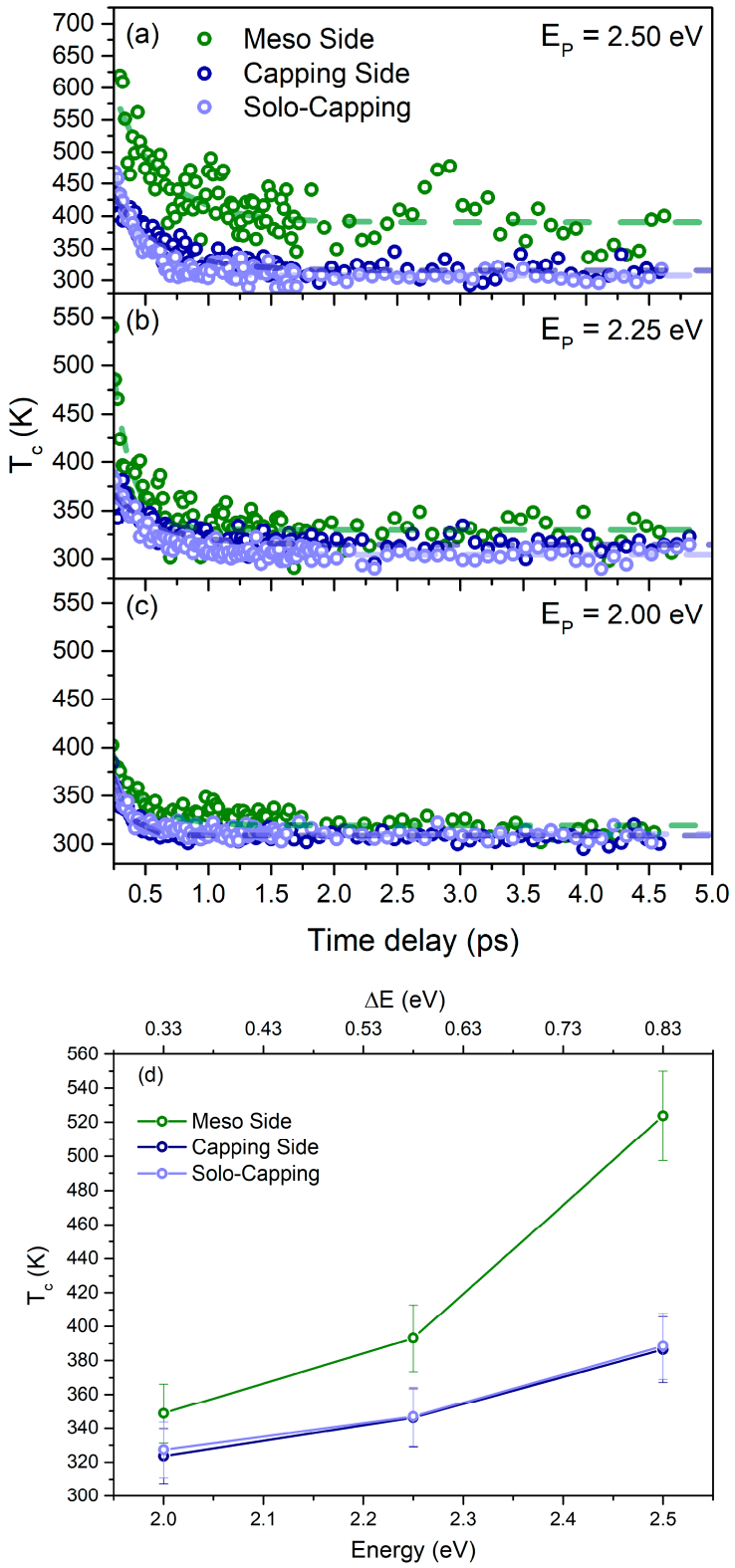

Figure 5. T_C as a function of time delay estimated for the Meso-Capping sample illuminated from the Meso and Capping sides and for the Solo-Capping sample acquired with E_p at (**a**) 2.50 eV, (**b**) 2.25 eV and (**c**) 2.00 eV. (**d**) T_C as a function of pump energy estimated for the Meso-Capping sample illuminated from the Meso and Capping sides and for the Solo-Capping sample obtained at a time delay of 400 fs.

3.3. Thermalization in Mesoporous Layer

In the light of these last observations, it is clear that in order to observe the effects of carrier thermalization it is necessary to examine the line shape of the TA signals at time delays shorter than 200 fs. The TA signals observed at a time delay of 100 fs by exciting the Meso-Capping sample at different pump energies from the Meso side are reported in Figure 6. In particular, the TA spectra (collected with the E_p = 3.00 eV, 2.50 eV and 2.25 eV at 100 fs of time delay) present a broad negative signal extending up to about 2.1 eV that can be correlated with the high-energy and non-thermal distribution of excited carriers. In fact, the shorter width and extension of this signal for the TA spectrum acquired with E_p = 2.25 eV with respect to that obtained at higher energy (2.50 eV), is justified by the smaller excess energy supplied by the pump with respect to the gap that induces a less extended energy distribution of the carriers. On the other hand, the TA spectrum obtained with the use of E_p = 3.00 eV presents a broad negative signal that extends only to slightly higher energies than that obtained with E_p = 2.50 eV. This small difference, not proportional to the energy difference of the pumps employed and much smaller than expected, can be explained by introducing a second gap at higher energies that induces a further singularity in the joint density of states that causes a change of the amplitude of the energy distribution of the carriers in the conduction band [32]. The data presented in Figure 6 were acquired using pump fluences one order of magnitude more intense than those used in the rest of this work with the aim of increasing the signal-to-noise ratio to allow an adequate analysis of the TA spectra. In any case, the measurements performed with the lower fluences (data not shown) are in agreement with the presented data. Moreover, the absence of this feature in the TA spectra acquired from the two capping layers suggests that the thermalization and cooling process, responsible for the energy redistribution between highly excited carriers, is faster in the capping layer (large crystals) than in the mesoporous layer (small crystals), in agreement with the discussion about T_C dynamics. In fact, the processes occurring below 200 fs present time constants comparable or even lower than the experimental IRF, preventing the temporal analysis of the dynamics of these features in the case of the small crystals or even being observed in the case of the large crystals.

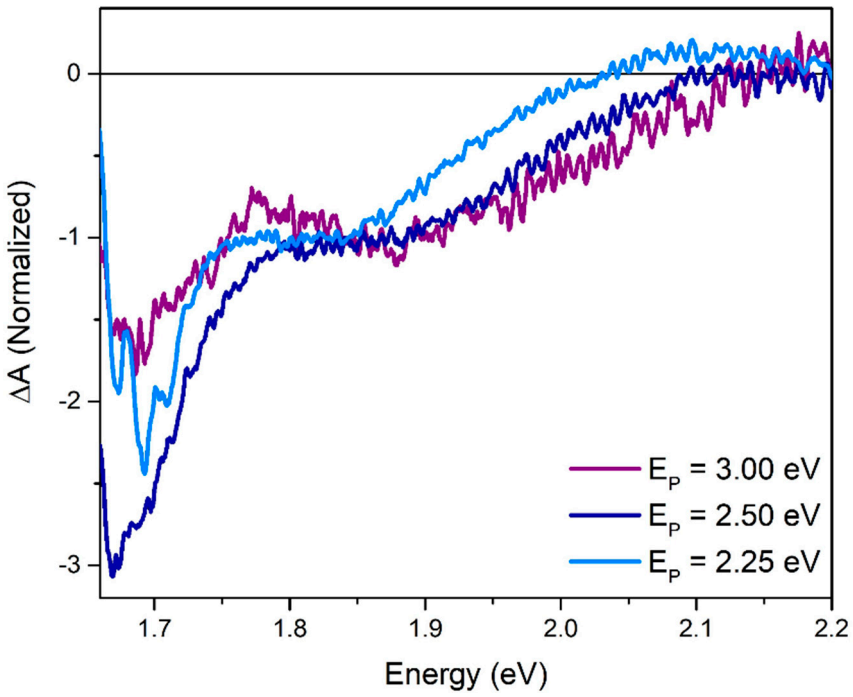

Figure 6. TA spectra of the Meso-Capping sample illuminated from the Meso side at selected E_p (3.00 eV, 2.50 eV and 2.25 eV), obtained at 100 fs of time delay.

4. Conclusions

In conclusion, we have performed fast transient absorbance spectroscopy measurements on mixed-cation hybrid lead halide perovskite samples investigating how the sizes and the morphology of the perovskite crystals embedded in the capping (large crystals) and mesoporous (small crystals) layer affect the temporal dynamics of the thermalization and cooling processes of the excited hot-carriers. The present study was performed on samples with the same layer design and thickness of a solar cell device using excitation energies in a wide visible spectral range with the aim of probing the material response in different excitation conditions and in a regime that mostly resembles that under sun illumination, as far as a pulsed excitation can do. Moreover, this work has demonstrated how to investigate different perovskite crystal structures embedded in the same sample, simply by illuminating its Mesoporous and Capping side and tuning the pump photon energy and thus the material penetration depth of the excitation pulse in a pump-probe configuration experiment. In this way, we have selectively followed the carrier temperature dynamics in the first hundreds of femtoseconds as a function of the excitation energy, shedding light on how the structure and morphology of the perovskite crystals can induce different rates of the carrier–carrier (thermalization) and carrier–phonon (cooling) scattering processes.

The comparative study between samples with perovskite deposited on substrates with and without the mesoporous layer has shown how the small crystals preserve the temperature of the carriers for a longer time after the excitation than the large crystals. This study showed how the high sensitivity of the time-resolved spectroscopies in discriminating the transient response due to the different morphology of the crystals embedded in the layers of the same sample can be applied in the characterization of solar cell devices and large area modules in operation, with the aim of investigating the dynamics of excited carriers under real working conditions and providing further and valuable information for the optimization and enhancement of the stability and the efficiency in power conversion of new perovskite-based devices. Notably, since the investigated cell structure and layer thickness are actually employed in large area modules, this study demonstrates how fast transient spectroscopy can be a valid tool for the characterization of marketable devices.

Author Contributions: Conceptualization, D.C., P.O., F.M. and S.T.; investigation, D.C., G.A., P.O., L.D.M., A.P., A.A. and S.P.; data curation and formal analysis, D.C., G.A. and F.T.; resources, A.A., S.P. and A.D.C.; writing—original draft preparation, D.C.; writing—review and editing, D.C., P.O., F.M., S.T., A.A., S.P. and A.D.C.; visualization, D.C and G.A. All authors have read and agreed to the published version of the manuscript.

Funding: This research received no external funding.

Institutional Review Board Statement: Not applicable.

Informed Consent Statement: Not applicable.

Data Availability Statement: Data is contained within the article.

Conflicts of Interest: The authors declare no conflict of interest.

References

1. Bi, Y.; Hutter, E.M.; Fang, Y.; Dong, Q.; Huang, J.; Savenije, T.J. Charge Carrier Lifetimes Exceeding 15 Ms in Methylammonium Lead Iodide Single Crystals. *J. Phys. Chem. Lett.* **2016**, *7*, 923–928. [CrossRef] [PubMed]
2. Stranks, S.D.; Eperon, G.E.; Grancini, G.; Menelaou, C.; Alcocer, M.J.P.; Leijtens, T.; Herz, L.M.; Petrozza, A.; Snaith, H.J. Electron-Hole Diffusion Lengths Exceeding 1 Micrometer in an Organometal Trihalide Perovskite Absorber. *Science* **2013**, *342*, 341–344. [CrossRef] [PubMed]
3. Manser, J.S.; Christians, J.A.; Kamat, P.V. Intriguing Optoelectronic Properties of Metal Halide Perovskites. *Chem. Rev.* **2016**, *116*, 12956–13008. [CrossRef] [PubMed]
4. Brenner, T.M.; Egger, D.A.; Kronik, L.; Hodes, G.; Cahen, D. Hybrid Organic—Inorganic Perovskites: Low-Cost Semiconductors with Intriguing Charge-Transport Properties. *Nat. Rev. Mater.* **2016**, *1*, 15007. [CrossRef]
5. Green, M.A.; Ho-Baillie, A. Perovskite Solar Cells: The Birth of a New Era in Photovoltaics. *ACS Energy Lett.* **2017**, *2*, 822–830. [CrossRef]

6. Kojima, A.; Teshima, K.; Shirai, Y.; Miyasaka, T. Novel Photoelectrochemical Cell with Mesoscopic Electrodes Sensitized by Lead-Halide Compounds (5). In *ECS Meeting Abstracts*; IOP Publishing: Bristol, UK, 2007. [CrossRef]
7. Available online: https://www.nrel.gov/pv/cell-efficiency.html (accessed on 1 December 2020).
8. Burschka, J.; Pellet, N.; Moon, S.-J.; Humphry-Baker, R.; Gao, P.; Nazeeruddin, M.K.; Grätzel, M. Sequential Deposition as a Route to High-Performance Perovskite-Sensitized Solar Cells. *Nature* **2013**, *499*, 316–319. [CrossRef]
9. Zhang, H.; Ren, X.; Chen, X.; Mao, J.; Cheng, J.; Zhao, Y.; Liu, Y.; Milic, J.; Yin, W.-J.; Grätzel, M.; et al. Improving the Stability and Performance of Perovskite Solar Cells via Off-the-Shelf Post-Device Ligand Treatment. *Energy Environ. Sci* **2018**, *11*, 2253–2262. [CrossRef]
10. Jena, A.K.; Kulkarni, A.; Miyasaka, T. Halide Perovskite Photovoltaics: Background, Status, and Future Prospects. *Chem. Rev.* **2019**, *119*, 3036–3103. [CrossRef]
11. Brunetti, B.; Cavallo, C.; Ciccioli, A.; Gigli, G.; Latini, A. On the Thermal and Thermodynamic (In)Stability of Methylammonium Lead Halide Perovskites. *Sci. Rep.* **2016**, *6*, 31896. [CrossRef]
12. Saliba, M.; Matsui, T.; Seo, J.-Y.; Domanski, K.; Correa-Baena, J.-P.; Nazeeruddin, M.K.; Zakeeruddin, S.M.; Tress, W.; Abate, A.; Hagfeldt, A.; et al. Cesium-Containing Triple Cation Perovskite Solar Cells: Improved Stability, Reproducibility and High Efficiency. *Energy Environ. Sci.* **2016**, *9*, 1989–1997. [CrossRef]
13. Manser, J.S.; Kamat, P.V. Band Filling with Free Charge Carriers in Organometal Halide Perovskites. *Nat. Photonics* **2014**, *8*, 737–743. [CrossRef]
14. Ponseca, C.S.; Savenije, T.J.; Abdellah, M.; Zheng, K.; Yartsev, A.; Pascher, T.; Harlang, T.; Chabera, P.; Pullerits, T.; Stepanov, A.; et al. Organometal Halide Perovskite Solar Cell Materials Rationalized: Ultrafast Charge Generation, High and Microsecond-Long Balanced Mobilities, and Slow Recombination. *J. Am. Chem. Soc.* **2014**, *136*, 5189–5192. [CrossRef] [PubMed]
15. O'Keeffe, P.; Catone, D.; Paladini, A.; Toschi, F.; Turchini, S.; Avaldi, L.; Martelli, F.; Agresti, A.; Pescetelli, S.; Del Rio Castillo, A.E.; et al. Graphene-Induced Improvements of Perovskite Solar Cell Stability: Effects on Hot-Carriers. *Nano Lett.* **2019**, *19*, 684–691. [CrossRef] [PubMed]
16. Li, C.; Wang, A.; Deng, X.; Wang, S.; Yuan, Y.; Ding, L.; Hao, F. Insights into Ultrafast Carrier Dynamics in Perovskite Thin Films and Solar Cells. *ACS Photonics* **2020**, *7*, 1893–1907. [CrossRef]
17. Richter, J.M.; Branchi, F.; Valduga de Almeida Camargo, F.; Zhao, B.; Friend, R.H.; Cerullo, G.; Deschler, F. Ultrafast Carrier Thermalization in Lead Iodide Perovskite Probed with Two-Dimensional Electronic Spectroscopy. *Nat. Commun.* **2017**, *8*, 376. [CrossRef]
18. Li, M.; Bhaumik, S.; Goh, T.W.; Kumar, M.S.; Yantara, N.; Grätzel, M.; Mhaisalkar, S.; Mathews, N.; Sum, T.C. Slow Cooling and Highly Efficient Extraction of Hot Carriers in Colloidal Perovskite Nanocrystals. *Nat. Commun.* **2017**, *8*, 14350. [CrossRef]
19. Li, M.; Fu, J.; Xu, Q.; Sum, T.C. Slow Hot-Carrier Cooling in Halide Perovskites: Prospects for Hot-Carrier Solar Cells. *Adv. Mater.* **2019**, *31*, 1802486. [CrossRef]
20. Kahmann, S.; Loi, M.A. Hot Carrier Solar Cells and the Potential of Perovskites for Breaking the Shockley–Queisser Limit. *J. Mater. Chem. C* **2019**, *7*, 2471–2486. [CrossRef]
21. Yang, J.; Wen, X.; Xia, H.; Sheng, R.; Ma, Q.; Kim, J.; Tapping, P.; Harada, T.; Kee, T.W.; Huang, F.; et al. Acoustic-Optical Phonon up-Conversion and Hot-Phonon Bottleneck in Lead-Halide Perovskites. *Nat. Commun.* **2017**, *8*, 14120. [CrossRef]
22. Yang, Y.; Ostrowski, D.P.; France, R.M.; Zhu, K.; van de Lagemaat, J.; Luther, J.M.; Beard, M.C. Observation of a Hot-Phonon Bottleneck in Lead-Iodide Perovskites. *Nat. Photonics* **2016**, *10*, 53–59. [CrossRef]
23. Guo, Z.; Wan, Y.; Yang, M.; Snaider, J.; Zhu, K.; Huang, L. Long-Range Hot-Carrier Transport in Hybrid Perovskites Visualized by Ultrafast Microscopy. *Science* **2017**, *356*, 59–62. [CrossRef] [PubMed]
24. Fang, H.-H.; Adjokatse, S.; Shao, S.; Even, J.; Loi, M.A. Long-Lived Hot-Carrier Light Emission and Large Blue Shift in Formamidinium Tin Triiodide Perovskites. *Nat. Commun.* **2018**, *9*, 243. [CrossRef] [PubMed]
25. Pasanen, H.P.; Vivo, P.; Canil, L.; Hempel, H.; Unold, T.; Abate, A.; Tkachenko, N.V. Monitoring Charge Carrier Diffusion across a Perovskite Film with Transient Absorption Spectroscopy. *J. Phys. Chem. Lett.* **2020**, *11*, 445–450. [CrossRef] [PubMed]
26. Baumeler, T.; Arora, N.; Hinderhofer, A.; Akin, S.; Greco, A.; Abdi-Jalebi, M.; Shivanna, R.; Uchida, R.; Liu, Y.; Schreiber, F.; et al. Minimizing the Trade-Off between Photocurrent and Photovoltage in Triple-Cation Mixed-Halide Perovskite Solar Cells. *J. Phys. Chem. Lett.* **2020**, *11*, 10188–10195. [CrossRef] [PubMed]
27. Wang, T.; Jin, L.; Hidalgo, J.; Chu, W.; Snaider, J.M.; Deng, S.; Zhu, T.; Lai, B.; Prezhdo, O.; Correa-Baena, J.-P.; et al. Protecting Hot Carriers by Tuning Hybrid Perovskite Structures with Alkali Cations. *Sci. Adv.* **2020**, *6*, eabb1336. [CrossRef] [PubMed]
28. Understanding the Interfaces between Triple-Cation Perovskite and Electron or Hole Transporting Material | ACS Applied Materials & Interfaces. Available online: https://pubs.acs.org/doi/10.1021/acsami.0c07095 (accessed on 21 January 2021).
29. Agresti, A.; Pazniak, A.; Pescetelli, S.; Di Vito, A.; Rossi, D.; Pecchia, A.; Auf der Maur, M.; Liedl, A.; Larciprete, R.; Kuznetsov, D.V.; et al. Titanium-Carbide MXenes for Work Function and Interface Engineering in Perovskite Solar Cells. *Nat. Mater.* **2019**, *18*, 1228–1234. [CrossRef]
30. Zhao, X.; Tao, L.; Li, H.; Huang, W.; Sun, P.; Liu, J.; Liu, S.; Sun, Q.; Cui, Z.; Sun, L.; et al. Efficient Planar Perovskite Solar Cells with Improved Fill Factor via Interface Engineering with Graphene. *Nano Lett.* **2018**, *18*, 2442–2449. [CrossRef]
31. Yang, G.; Chen, C.; Yao, F.; Chen, Z.; Zhang, Q.; Zheng, X.; Ma, J.; Lei, H.; Qin, P.; Xiong, L.; et al. Effective Carrier-Concentration Tuning of SnO_2 Quantum Dot Electron-Selective Layers for High-Performance Planar Perovskite Solar Cells. *Adv. Mater.* **2018**, *30*, 1706023. [CrossRef]

32. Anand, B.; Sampat, S.; Danilov, E.O.; Peng, W.; Rupich, S.M.; Chabal, Y.J.; Gartstein, Y.N.; Malko, A.V. Broadband Transient Absorption Study of Photoexcitations in Lead Halide Perovskites: Towards a Multiband Picture. *Phys. Rev. B* **2016**, *93*, 161205. [CrossRef]
33. Polyakov, A.Y.; Smirnov, N.B.; Shchemerov, I.V.; Saranin, D.S.; Le, T.S.; Didenko, S.I.; Kuznetsov, D.V.; Agresti, A.; Pescetelli, S.; Matteocci, F.; et al. Trap States in Multication Mesoscopic Perovskite Solar Cells: A Deep Levels Transient Spectroscopy Investigation. *Appl. Phys. Lett.* **2018**, *113*, 263501. [CrossRef]
34. Noël, C.; Pescetelli, S.; Agresti, A.; Franquet, A.; Spampinato, V.; Felten, A.; di Carlo, A.; Houssiau, L.; Busby, Y. Hybrid Perovskites Depth Profiling with Variable-Size Argon Clusters and Monatomic Ions Beams. *Materials* **2019**, *12*, 726. [CrossRef] [PubMed]
35. Catone, D.; Di Mario, L.; Martelli, F.; O'Keeffe, P.; Paladini, A.; Stefano Pelli Cresi, J.; Sivan, A.K.; Tian, L.; Toschi, F.; Turchini, S. Ultrafast Optical Spectroscopy of Semiconducting and Plasmonic Nanostructures and Their Hybrids. *Nanotechnology* **2020**, *32*, 025703. [CrossRef] [PubMed]
36. Toschi, F.; Catone, D.; O'Keeffe, P.; Paladini, A.; Turchini, S.; Dagar, J.; Brown, T.M. Enhanced Charge Separation Efficiency in DNA Templated Polymer Solar Cells. *Adv. Funct. Mater.* **2018**, *28*, 1707126. [CrossRef]
37. Rossi, G.; Pasquini, L.; Catone, D.; Piccioni, A.; Patelli, N.; Paladini, A.; Molinari, A.; Caramori, S.; O'Keeffe, P.; Boscherini, F. Charge Carrier Dynamics and Visible Light Photocatalysis in Vanadium-Doped TiO2 Nanoparticles. *Appl. Catal. B Environ.* **2018**, *237*, 603–612. [CrossRef]
38. De Wolf, S.; Holovsky, J.; Moon, S.-J.; Löper, P.; Niesen, B.; Ledinsky, M.; Haug, F.-J.; Yum, J.-H.; Ballif, C. Organometallic Halide Perovskites: Sharp Optical Absorption Edge and Its Relation to Photovoltaic Performance. *J. Phys. Chem. Lett.* **2014**, *5*, 1035–1039. [CrossRef]
39. Tan, H.; Che, F.; Wei, M.; Zhao, Y.; Saidaminov, M.I.; Todorović, P.; Broberg, D.; Walters, G.; Tan, F.; Zhuang, T.; et al. Dipolar Cations Confer Defect Tolerance in Wide-Bandgap Metal Halide Perovskites. *Nat. Commun.* **2018**, *9*, 3100. [CrossRef] [PubMed]
40. Cacovich, S.; Messou, D.; Bercegol, A.; Béchu, S.; Yaiche, A.; Shafique, H.; Rousset, J.; Schulz, P.; Bouttemy, M.; Lombez, L. Light-Induced Passivation in Triple Cation Mixed Halide Perovskites: Interplay between Transport Properties and Surface Chemistry. *ACS Appl. Mater. Interfaces* **2020**, *12*, 34784–34794. [CrossRef]
41. Andaji-Garmaroudi, Z.; Abdi-Jalebi, M.; Guo, D.; Macpherson, S.; Sadhanala, A.; Tennyson, E.M.; Ruggeri, E.; Anaya, M.; Galkowski, K.; Shivanna, R.; et al. A Highly Emissive Surface Layer in Mixed-Halide Multication Perovskites. *Adv. Mater.* **2019**, *31*, 1902374. [CrossRef]
42. Sum, T.C.; Mathews, N.; Xing, G.; Lim, S.S.; Chong, W.K.; Giovanni, D.; Dewi, H.A. Spectral Features and Charge Dynamics of Lead Halide Perovskites: Origins and Interpretations. *Acc. Chem. Res.* **2016**, *49*, 294–302. [CrossRef]
43. Lamanna, E.; Matteocci, F.; Calabrò, E.; Serenelli, L.; Salza, E.; Martini, L.; Menchini, F.; Izzi, M.; Agresti, A.; Pescetelli, S.; et al. Mechanically Stacked, Two-Terminal Graphene-Based Perovskite/Silicon Tandem Solar Cell with Efficiency over 26%. *Joule* **2020**, *4*, 865–881. [CrossRef]
44. Agresti, A.; Pescetelli, S.; Palma, A.L.; Martín-García, B.; Najafi, L.; Bellani, S.; Moreels, I.; Prato, M.; Bonaccorso, F.; Di Carlo, A. Two-Dimensional Material Interface Engineering for Efficient Perovskite Large-Area Modules. *ACS Energy Lett.* **2019**, *4*, 1862–1871. [CrossRef]
45. Li, M.; Begum, R.; Fu, J.; Xu, Q.; Koh, T.M.; Veldhuis, S.A.; Grätzel, M.; Mathews, N.; Mhaisalkar, S.; Sum, T.C. Low Threshold and Efficient Multiple Exciton Generation in Halide Perovskite Nanocrystals. *Nat. Commun.* **2018**, *9*, 4197. [CrossRef] [PubMed]
46. Zhou, C.; Ou, Q.; Chen, W.; Gan, Z.; Wang, J.; Bao, Q.; Wen, X.; Jia, B. Illumination-Induced Halide Segregation in Gradient Bandgap Mixed-Halide Perovskite Nanoplatelets. *Adv. Opt. Mater.* **2018**, *6*, 1801107. [CrossRef]
47. Ou, Q.; Bao, X.; Zhang, Y.; Shao, H.; Xing, G.; Li, X.; Shao, L.; Bao, Q. Band Structure Engineering in Metal Halide Perovskite Nanostructures for Optoelectronic Applications. *Nano Mater. Sci.* **2019**, *1*, 268–287. [CrossRef]
48. Balandin, A.A.; Nika, D.L. Phononics in Low-Dimensional Materials. *Mater. Today* **2012**, *15*, 266–275. [CrossRef]
49. Hopper, T.R.; Gorodetsky, A.; Jeong, A.; Krieg, F.; Bodnarchuk, M.I.; Maimaris, M.; Chaplain, M.; Macdonald, T.J.; Huang, X.; Lovrincic, R.; et al. Hot Carrier Dynamics in Perovskite Nanocrystal Solids: Role of the Cold Carriers, Nanoconfinement, and the Surface. *Nano Lett.* **2020**, *20*, 2271–2278. [CrossRef]
50. Fu, J.; Xu, Q.; Han, G.; Wu, B.; Huan, C.H.A.; Leek, M.L.; Sum, T.C. Hot Carrier Cooling Mechanisms in Halide Perovskites. *Nat. Commun.* **2017**, *8*, 1300. [CrossRef]
51. Ghosh, T.; Aharon, S.; Etgar, L.; Ruhman, S. Free Carrier Emergence and Onset of Electron–Phonon Coupling in Methylammonium Lead Halide Perovskite Films. *J. Am. Chem. Soc.* **2017**, *139*, 18262–18270. [CrossRef]